RSC Advances

PAPER

View Article Online
View Journal | View Issue

Cite this: *RSC Adv.*, 2025, **15**, 15252

Layer-by-layer assembly of tetra-Mn-containing 30-tungsto-4-phosphate, $[M_4(H_2O)_2(P_2W_{15}O_{56})_2]^{n-}$ (M = Mn^{II} and Mn^{III}) with AuNps-MWCNT: electrochemical detection of iodate†

Suganya Pitchai Muthusamy, Indherjith Sakthinathan and Timothy McCormac *

This study demonstrates the Layer-by-Layer (LbL) approach to assemble the sandwich structured $[M_4(H_2O)_2(P_2W_{15}O_{56})_2]^{n-}$ (M = Mn^{II} and Mn^{III}) polyoxometalates (POMs) with gold nanoparticles (AuNps) decorated multi-walled carbon nanotubes (MWCNT) on a carbon electrode. Polyethylenimine has been employed as a base layer prior to the deposition of the AuNps-MWCNT and POM. The multi-layered modified electrodes [AuNps-MWCNT/$Mn^{II}(P_2W_{15})_2$] and [AuNps-MWCNT/$Mn^{III}(P_2W_{15})_2$] have been characterised using electrochemical and surface techniques. Electrochemical impedance spectroscopy data revealed that the addition of AuNps-MWCNT increased the multilayer films' conductivity. The modified electrodes displayed pH dependent redox activity associated with the POM and thin-layer behaviour, as demonstrated by cyclic voltammetry (CV). The stability of the multilayer towards redox cycling through the POM redox processes was found to be good along with the ability of the modified electrode towards the electrocatalytic reduction of iodate. The amperometric investigation of AuNps-MWCNT/$Mn^{II}(P_2W_{15})_2$ multilayer films revealed a linear range of 1–3000 μM with the limit of detection (LOD) and sensitivity was found to be 0.14 μM (S/N = 3) and 0.58 μA cm^{-2} μM^{-1}. Similarly, the AuNps-MWCNT/$Mn^{III}(P_2W_{15})_2$ multilayer films showed a linear range of 1–3000 μM with a limit of detection and sensitivity was found to be 0.20 μM (S/N = 3) and 0.90 μA cm^{-2} μM^{-1}.

Received 4th March 2024
Accepted 5th February 2025

DOI: 10.1039/d4ra01691b

rsc.li/rsc-advances

1. Introduction

Polyoxometalates (POMs) are a class of discrete inorganic anionic metal-oxide clusters, mostly early transition metals (V, Nb, Ta, Mo, W) in their highest oxidation state.[1,2] This group of inorganic compounds is exceptional not only in terms of structural variety, for instance, their monodisperse size can be selectively tuned from several angstroms to 10 nm, charge distribution, but also in terms of selectivity and relevance to analytical chemistry,[3] catalysis,[4–6] photochemistry,[7,8] medicine,[9] and materials science.[6] Because their properties can be desirably tuned by picking and incorporating the right constituting elements, POMs are excellent candidates for designing electrocatalysts.[10] One of their most important properties is their ability to undergo reversible multivalence reductions/oxidations, resulting in the formation of mixed-valence species with favourable electrocatalytic properties in a variety of electrochemical processes.[11–13]

Hybrid nanocomposite based on inorganic nanoparticles (NPs) and graphene derivatives combines the unique properties such as larger surface area, optical and biological properties of inorganic NPs with outstanding properties of graphene derivatives, notably conductivity, stability, physical, chemical and mechanical characteristics allowing access to novel interesting multifunctionality for diverse technology purpose.[14–16] Gold nanoparticles (AgNps) decorated multiwalled carbon nanotube (MWCNT) show unique properties like high surface area energy, large surface area and functioning as an electron-conducting pathway to facilitate electron transfer between the redox materials and the bulk electrolyte.[14,17] It is well understood that the modification of electrode materials by combining the various synergistic properties of MWCNT-AuNPs with the redox properties of POM improves the performance of the electrochemical sensor.[18,19]

Recently, several strategies have been adopted to prepare POM-based nanostructured thin films on the surface of the electrodes, including POMs entrapped in polymers matrix,[20,21] self-organised hybrids based on POMs and cationic surfactants, Langmuir–Blodgett technique,[22,23] layer-by-layer self-assembly method,[24–26] and other approaches.[27–29] Layer-by-Layer (LbL) assembly is a widely used technique and is well known for its simplicity, control over the thickness by adjusting the number of deposited layers, high stability, high mechanical strength, uniform morphology, and good permeability to small molecules.[30,31] The complementary forces are not only electrostatic and van der Waals

Electrochemistry Research Group, Department of Applied Science, Dundalk Institute of Technology, Dublin Road Dundalk-A91 K584, County Louth, Ireland. E-mail: tim.mccormac@dkit.ie

† Electronic supplementary information (ESI) available. See DOI: https://doi.org/10.1039/d4ra01691b

but also include hydrogen bonding, bio-specific interactions, metal coordination, charge transfer, *etc.*[29] LbL is compatible with other branches of chemistry, meaning that a wide variety of different surfaces can be coated. It involves the sequential assembly of the layers and a washing step after the addition of each layer to remove the excess non-assembled materials and/or molecules. LbL enables convenient surface chemistry tailoring because of the large variety of materials and substrates that can be used to construct multifunctional devices.[32,33] Moreover, the LbL method replicates the essential aspects of physics and chemistry of material engineering in living organisms, leading to an amazing spectrum of biomimetic materials.[34,35]

Iodine is a crucial micronutrient that aids in the development of both neurological activity and cell proliferation. A significant delay in neurologic development may be caused by thyroid hormone deficiency.[36,37] For instance, in many nations, iodized salt is the best method for preventing iodine deficiency disorder. However, too much iodine or iodide can result in hyperthyroidism, goitre, and hypothyroidism.[38–40] Periodate is a powerful oxidant capable of oxidizing a wide range of inorganic and organic substances at extremely low concentrations. As a result, iodine detection is critical in many areas, including food, medicine, and industry. Nanoparticles modified electrodes[41,42] and graphene derivatives[43] modified electrodes have been employed as electrochemical sensors for the detection of iodate. The PEI/rGO-Au@P_8W_{48} composite film-modified electrode that was reported by Xiaoxia Zhang *et al.* combines the excellent catalytic activity of the Au@P_8W_{48} with the superior conductivity of rGO, displaying a low detection limit, high sensitivity, good selectivity, and rapid response toward hydrogen peroxide.[44] A Dawson-type ($S_2W_{18}O_{62}$) POM-entrapped polypyrrole film was constructed on the surface of the GC electrode and has been utilised as an electrochemical sensor for iodate.[45] Minoo Sharifi *et al.* reported the amperometric detection of iodate using a multicomponent containing ionic liquid/$SiW_{11}O_{39}Ni(H_2O)$ POM/phosphorus-doped graphene oxide modified glassy carbon electrode.[46]

In this contribution, the LbL technique has been utilised to construct the multi-layered catalyst on the surface of the GCE by alternative deposition of MWCNT-AuNps and $Mn^{II}_4(P_2W_{15}O_{56})_2$/or $Mn^{III}_4(P_2W_{15}O_{56})_2$ to the electrochemical detection of iodate. Utilizing cyclic voltammetric techniques (CV), the electrochemical behaviour of the multi-layered modified electrodes was investigated. When an electrode is modified with MWCNT-AuNps, it becomes more conductive, as demonstrated by electrochemical impedance spectroscopy (EIS).[47–49] Finally, the potential of multilayer-modified electrodes towards the detection of iodate was studied using voltammetric and chronoamperometric techniques. We believe that the synergistic effect of both AuNps-MWCNT and POM improved the electrochemical sensing activity.[44,46,50]

2. Experimental section

2.1. Materials

$Na_{12}P_2W_{15}O_{56}\cdot 18H_2O$[51] and $[Mn^{III}_8Mn^{IV}_4O_{12}(CH_3COO)_{16}(H_2O)_4]\cdot 2CH_3COOH\cdot 4H_2O$[52] have been synthesised using reported procedures. Multi-walled carbon nanotubes used in this study were purchased from Sigma Aldrich with a purity of 98% based on trace metal analysis, length of 2.5–20 microns, inner diameter of 2–6 nm, outer diameter of 6–13 nm, and a surface area of 216 $m^2\ g^{-1}$. Alumina powders of sizes 0.05, 0.3, and 1.0 μm were received from IJ Cambria. Highly purified water obtained using a Milli-Q water purification system (ELGA PURELAB Option-Q) with a resistivity of 18.2 MΩ cm was used throughout the preparation of all aqueous electrolytes and buffer solutions. All other chemicals were of reagent grade, purchased from Sigma Aldrich, and used as received. Buffer solutions were prepared from the following reagents: 0.1 M Na_2SO_4 (pH 2–3), 0.1 mmol L^{-1} Na_2SO_4 + 20 mmol L^{-1} CH_3COOH (pH 3.5–5), and 0.1 mmol L^{-1} Na_2SO_4 + 20 mmol L^{-1} NaH_2PO_4 (pH 5.5–7). The pH of the solutions was adjusted with either 0.1 M NaOH or 0.1 M H_2SO_4 depending on the pH required.

2.2. Synthesis of $Na_{16}[Mn^{II}_4(H_2O)_2(P_2W_{15}O_{56})_2]\cdot nH_2O$

The compound was synthesised using the reported procedure with slight modification[53] typically, 2.5 mmol L^{-1} of $MnCl_2\cdot 4H_2O$ (0.4948 g) was added to 50 mL of a 1 mol L^{-1} solution of NaCl, and then 4 g of $Na_{12}P_2W_{15}O_{56}\cdot 18H_2O$ was slowly added to the solution. The solution was heated at 50 °C for several minutes until the solution became transparent. The orange solution was warm-filtered through paper and allowed to crystallize at room temperature, resulting in the formation of orange rhombic prismatic crystals overnight. However, the solution was undisturbed for 2 days before filtration. These crystals, very soluble in water, were also recrystallized in water at room temperature.

2.3. Synthesis of $Na_{12}[Mn^{III}_4(H_2O)_2(P_2W_{15}O_{56})_2]\cdot 84H_2O$

$[Mn^{III}_8Mn^{IV}_4O_{12}(CH_3COO)_{16}(H_2O)_4]\cdot 2CH_3COOH\cdot 4H_2O$ (0.270 g, 0.128 mmol) was suspended in a mixture of 36 mL of CH_3CO_2H and 24 mL of H_2O (resulting in pH 1.1) for 1 h. To this solution, $Na_{12}[P_2W_{15}O_{56}]\cdot 18H_2O$ (1.104 g, 0.256 mmol) was added. After stirring for 30 min at room temperature, the mixture was heated to 80 °C for another 1 h and filtered. Then, NaCl (0.40 g, 6.87 mmol) was added to the solution. The filtrate was kept for crystallization at room temperature. Brown crystals were obtained after a few days.[44]

2.4. Synthesis of MWCNT

The gold-decorated MWCNT has been synthesised in three steps using the reported procedure.

Step 1. Synthesis of oxidised MWCNT 0.2 g of MWCNT was treated for 4 hours at 40 °C in a round bottom flask with a condenser containing 30 mL of a (3/1H_2SO_4/HNO_3 mixture), then diluted with 360 mL of distillate water and left overnight. Finally, the suspension was washed and dried in an oven at 50 °C to obtain the oxidised MWCNT (Ox-MWCNT).

Step 2. Thiolation of MWCNT: 22 mg of the Oxi-MWCNT, which was obtained from the first step, was treated with a solution of 27 mg of cysteamine chloride in 10 mL of distilled water at 90 °C for 30 h. After cooling to room temperature, the powder was washed with distilled water to remove the

unreacted excess of amine, followed by centrifugation at 12 000 rpm. The powder was dried under a vacuum for 14 hours to obtain the thiol-oxi-MWCNT. The degree of oxidation was estimated to be between 2 to 10% and similarly, the degree of thiolation to be 1 to 5% from the reported literature.[54,55]

Step 3. Preparation of an AuNps-decorated MWCNT: AuNps-decorated MWCNTs were synthesized as described in the reported literature. Accordingly, the particle size distribution ranges between 15 and 30 nm.[56] 0.01 M of $HAuCl_4$ was added to the thiolated MWCNT suspension, and the resulting suspension was sonicated for 30 min. Three equivalents of sodium citrate were introduced into the suspension and heated to 90 °C. Au III was reduced by sodium citrate solution, and Au NPs were gradually formed as the Au^{3+} changed to Au^0 according to the following reactions.

$$2HAuCL_4 + 4Na_3C_6H_5O_7 \rightarrow 2Au + 4NaCl + 4HCl + 4Na_2C_5H_4O_5 + 4CO_2 + H_2 \quad (1)$$

2.5. Instruments

All electrochemical experiments were performed with a CHI-660c electrochemical workstation (CH Instruments, Texas, IUPAC) with a conventional three-electrode electrochemical cell. The glassy carbon electrode (GCE) (d = 3 mm, geometric area = 0.0707 cm^2) was used as the working electrode, a platinum wire as the auxiliary electrode (length = 5 cm, d = 0.5 mm), and a Ag/AgCl (saturated KCl) as the reference electrode. AFM analyses were carried out using an NT-MDT SPM Solver P47H-PRO instrument operating in tapping mode and air.

2.6. Preparation of working electrode

The GCE was firstly polished with 1.0, 0.3, and 0.05 μm Al_2O_3 powders, and sonicated in water for about 10 s after each polishing step. Finally, the electrode was washed with ethanol and then dried with a nitrogen stream prior to use.

A monolayer of polyelectrolyte PEI was deposited onto the GCE to ensure an evenly charged surface. The polished and dried GCE was immersed in a 2% (w/w) PEI solution for 10 minutes to create the PEI coated electrode and was subsequently dried under nitrogen after being cleaned with deionized water to remove any excess PEI solution. The PEI-coated electrodes were dipped into a solution of MWCNT-AuNps for 20 min to form gold nanoparticles decorated multi-walled carbon nanotubes layer (Step 1) and then rinsed with deionized water to remove the unbounded materials and dried under a nitrogen stream (Step 2). Then MWCNT-AuNps coated substrate was then immersed in a 1 mmol L^{-1} solution of $Mn^{II}(P_2W_{15})_2$/or $Mn^{III}(P_2W_{15})_2$ POM for 20 min to create a POM layer (Step 3) and then washed with deionized water and dried under nitrogen (Step 4). Multilayers were then built up by alternating deposition of MWCNT-AuNps and POM solution until the desired number of layers was reached. Water rinsing and nitrogen stream drying steps were performed after each deposition step. An illustration of LbL film has been shown in Scheme 1.

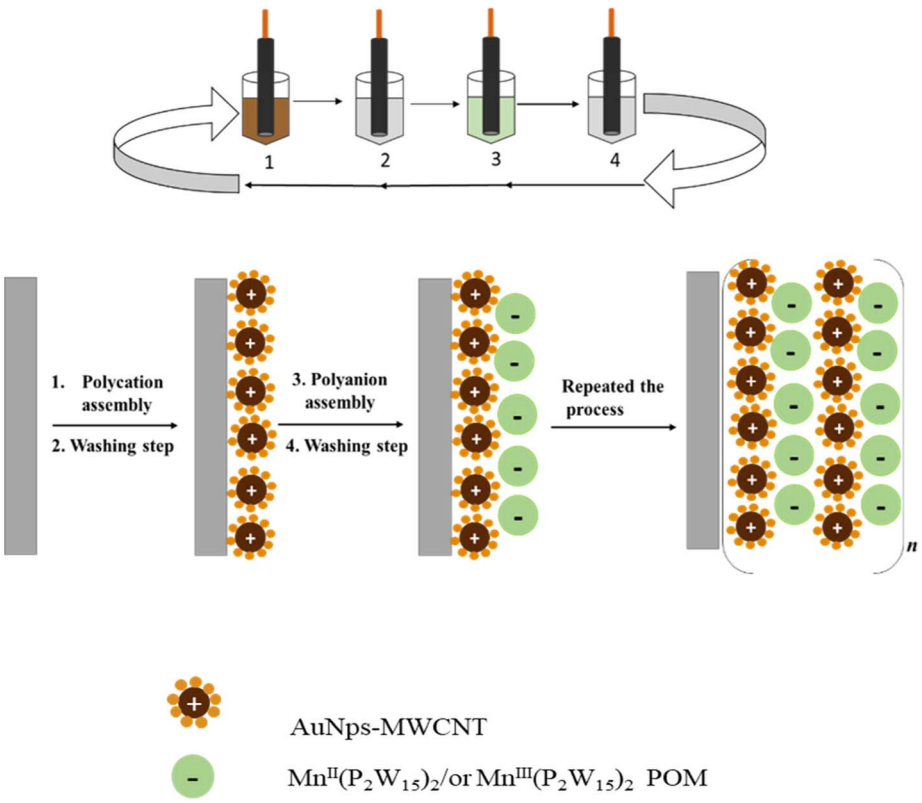

Scheme 1 Schematic representation of the layer-by-layer self-assembly method.

3. Results and discussion

3.1. Voltammetric behaviour of $Mn^{II}(P_2W_{15})_2$ and $Mn^{III}(P_2W_{15})_2$ in aqueous electrolyte

The electrochemical behaviour of $Mn^{II}(P_2W_{15})_2$ and $Mn^{III}(P_2W_{15})_2$ in the pH 2 buffer containing (0.1 mol L^{-1} Na_2SO_4) has been investigated using CV at a scan rate of 10 mV s^{-1}. Fig. 1(a) and (b) show the resulting cyclic voltammogram of the tungsten-oxo (W–O) units and the Mn^{III}/Mn^{II} in $Mn^{II}(P_2W_{15})_2$, respectively. Fig. 1(a) shows the presence of three well-defined redox peaks labelled as W–O I, II and III corresponding to the bielectronic redox process of the tungsten-oxo framework present in the $Mn^{II}(P_2W_{15})_2$ structure with the $E_{1/2}$ values of −0.367, −0.578, and −0.803 V *vs.* Ag/AgCl. The redox activity associated with the Mn(III/II)-oxo within the POM moiety was observed with an $E_{1/2}$ = +0.904 V (Fig. 1(b)).[57] Similarly, Fig. 1(c) shows the presence of four multiple electron well-defined redox couples I–IV, which are, associated with trilacunary $\{P_2W_{15}O_{56}\}$ Dawson units of the POM. Redox process I is bielectronic in nature with an $E_{1/2}$ value of +0.008 mV, whilst processes II and III have $E_{1/2} = -0.128$ mV and −0.223 mV, respectively, are mono-electronic as reported from the previous literature. Redox process IV with an $E_{1/2} = -0.5$ mV is bielectronic. The redox activity associated with the Mn(IV/III)-oxo within the POM moiety is shown in Fig. 1(d) with an observed $E_{1/2}$ value of +1.124 V.[58]

3.2. Voltammetric behaviour of AuNps-MWCNT/$Mn^{II}_4(P_2W_{15})_2$ and AuNps-MWCNT/$Mn^{III}_4(P_2W_{15})_2$ multi-layered film

Fig. 2a and b show the CVs of 4 bilayers of AuNps-MWCNT/$Mn^{II}_4(P_2W_{15})_2$ and AuNps-MWCNT/$Mn^{III}_4(P_2W_{15})_2$ film-modified electrodes respectively, in the buffer system of pH 2

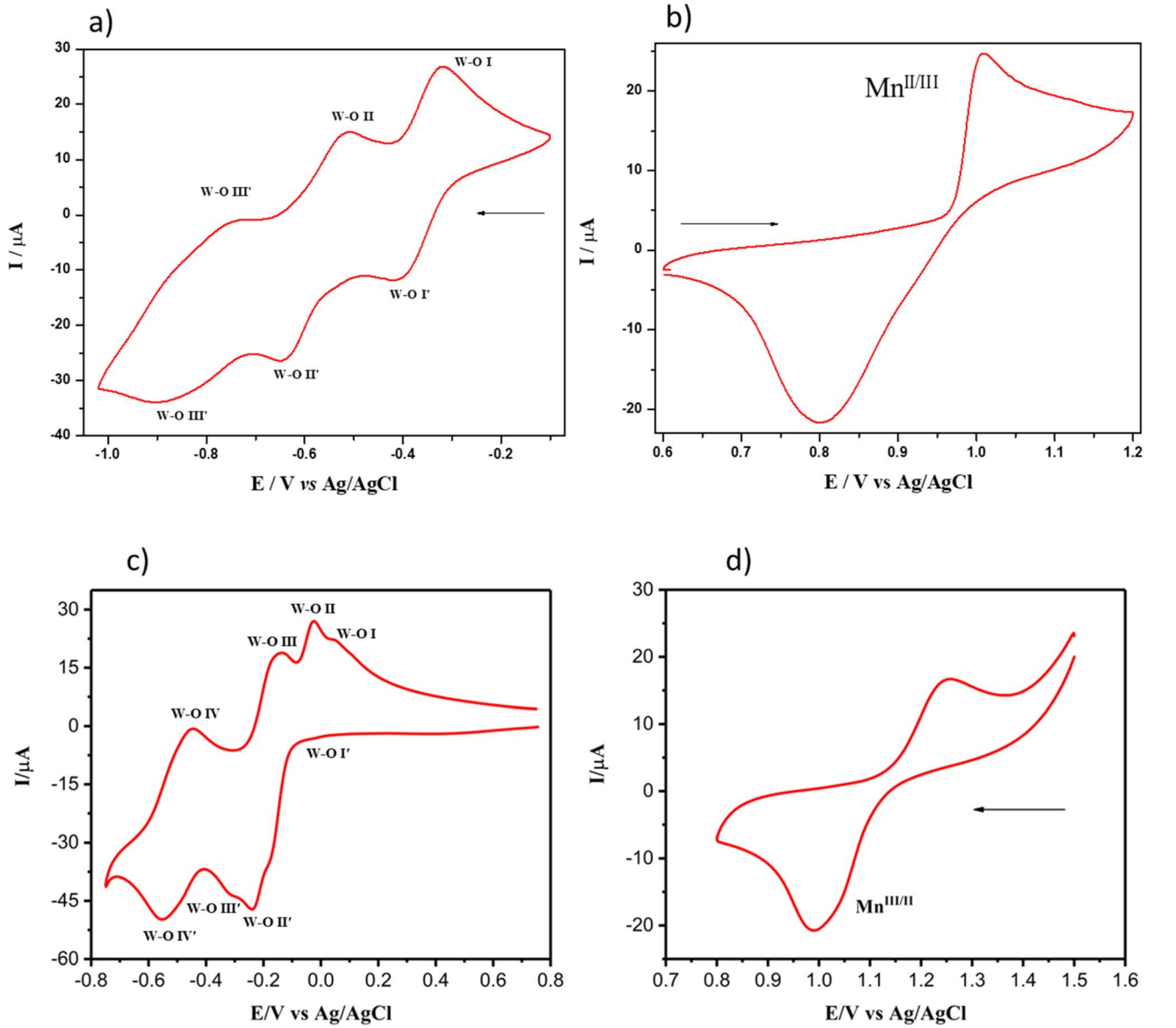

Fig. 1 Cyclic voltammograms of a 1 mM solution of (a) and (b) $Mn^{II}_4(P_2W_{15})_2$. (c) and (d) $Mn^{III}_4(P_2W_{15})_2$. (a) and (c) Restricted redox peaks of tungsten-oxo units. (b) and (d) Restricted redox couple of the Mn. Scan rate: 10 mV s^{-1}.

at the scan rate of 100 mV s^{-1}. The multilayer was constructed using the procedure given in Section 2.6. The figure illustrates that the magnitude of the anodic and cathodic peak currents increases with the number of bilayers. This indicates a progressive increase in the amount of material adsorbed onto the electrode surface with each deposition stage. As we can see from Fig. 2(a) and (b), three well-defined bielectronic reversible redox waves were observed which corresponds to the W–O species present in the $\{P_2W_{15}O_{56}\}$ Dawson units of the POM. The $E_{1/2}$ values of peak W–O I, W–O II, and W–O III were found to be −0.13, −0.29 and −0.62 V *vs.* Ag/AgCl for the $[AuNps\text{-}MWCNT/Mn^{II}{}_4(P_2W_{15})_2]_4$ and −0.14, −0.32 and −0.64 V *vs.* Ag/AgCl for the $[AuNps\text{-}MWCNT/Mn^{III}{}_4(P_2W_{15})_2]_4$ modified electrodes, respectively. Noteworthy, the intensity of the peak W–O I was less than the other two peaks observed in both the modified electrodes (Fig. 2a and b). Interestingly no redox activity was associated with the POM's manganese redox process observed in Fig. 1b and c. This could be ascribed to a possible ion exchange between the Mn and H^+ and Na^+ from the buffer solution as reported in the literature.[59] The two-electron transfer processes occur at each redox peak in the AuNps-MWCNT/$Mn^{II}{}_4(P_2W_{15})_2$ and AuNps-MWCNT/$Mn^{III}{}_4(P_2W_{15})_2$ film-modified electrodes, as shown in eqn (2)–(4) as from the reported literature.[59] Furthermore, As the layer increases the electrochemically active surface area increases because of an increase in the surface inhomogeneity. Which was observed in the previously reported literature.[29]

$$[P_2W_{15}O_{56}]^{n-} + 2e^- + 2H^+ \leftrightarrow [H_2P_2W_{15}O_{56}]^{n-} \quad (2)$$

$$[H_2P_2W_{15}O_{56}]^{n-} + 2e^- + 2H^+ \leftrightarrow [H_4P_2W_{15}O_{56}]^{n-} \quad (3)$$

$$[H_4P_2W_{15}O_{56}]^{n-} + 2e^- + 2H^+ \leftrightarrow [H_6P_2W_{15}O_{56}]^{n-} \quad (4)$$

To understand the electron transfer kinetics of the POM deposited on the surface of the modified electrodes, cyclic voltammogram of AuNps-MWCNT/$Mn^{II}{}_4(P_2W_{15})_2$ and AuNps-MWCNT/$Mn^{III}{}_4(P_2W_{15})_2$ modified electrode were recorded at different scan rates from 10 mV s^{-1} to 100 mV s^{-1} in pH 2 buffer (Fig. 3a and c). For electrochemically reversible electron transfer processes involving electrode-adsorbed redox species, the Randles–Sevcik equation (eqn (5))[60] describes how the peak current i_p (A) increases linearly with the scan rate ν (V s^{-1}).

$$i_p = \frac{n^2F^2}{4RT}\nu A\Gamma^* \quad (5)$$

where n is the number of electrons transferred in the redox event, A (cm^2) is the electrode surface area (usually treated as the geometric surface area), Γ^* is the surface coverage of the adsorbed species in mol cm^{-2}.

Fig. 3(a) and (c) show the linear increase in the peak current as the scan rate increases indicate the electron transfer in the multi-layered films should be adsorption/desorption-controlled rather than diffusion-controlled. Higher regression values and the slope values for the $[AuNps\text{-}MWCNT/Mn^{II}{}_4(P_2W_{15})_2]_4$ the $[AuNps\text{-}MWCNT/Mn^{III}{}_4(P_2W_{15})_2]_4$ multi-layered modified electrodes were calculated and listed in Table 1. The linear relationship between the peak currents (I_p) and the scan rate can be seen in Fig. 3(b) and (d).

The voltammetric behaviour of the POM-modified electrode is influenced by the acidity of the electrolyte solution due to the influence of the proton that is coupled with anionic POM and shifts its potential. To investigate the effect of pH of the electrolyte solution the CVs of $[AuNps\text{-}MWCNT/Mn^{II}{}_4(P_2W_{15})_2]_4$ and $[AuNps\text{-}MWCNT/Mn^{III}{}_4(P_2W_{15})_2]_4$ modified electrodes have been recorded in the electrolyte with range pH of 2–7 (Fig. 4a and c, respectively).

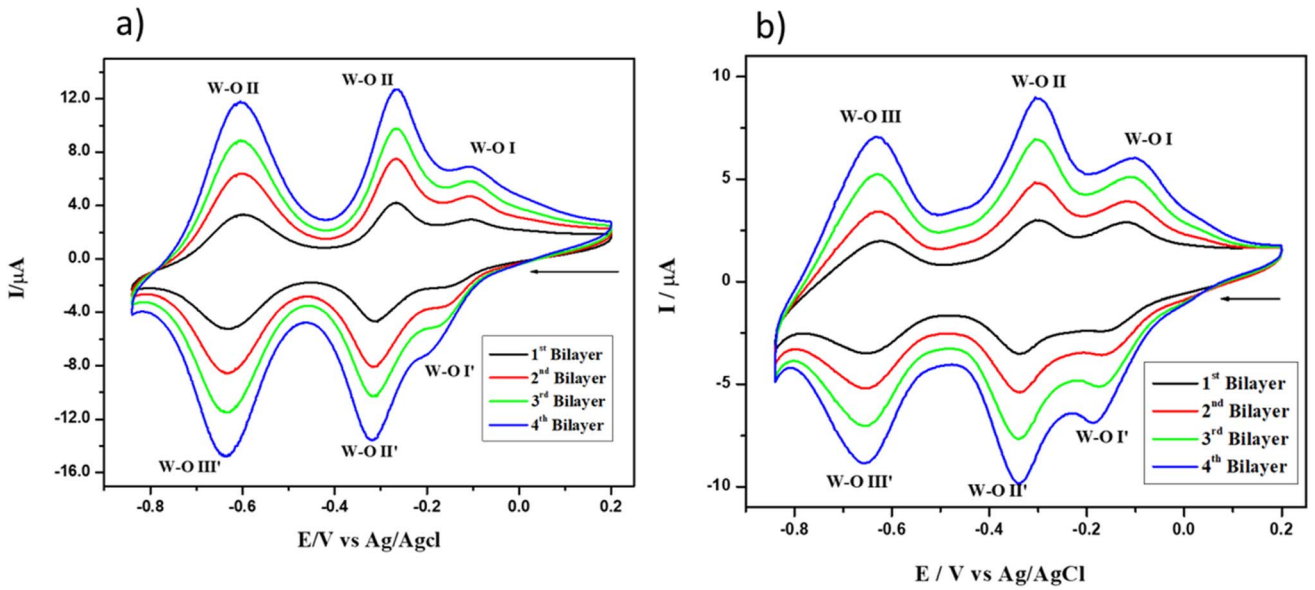

Fig. 2 CVs of multilayer modified GC electrode contains 4 bilayers of (a) AuNps-MWCNT/$Mn^{II}{}_4(P_2W_{15})_2$ and (b) AuNps-MWCNT/$Mn^{III}{}_4(P_2W_{15})_2$ at the scan rate of 100 mV s^{-1} in the pH 2 buffer.

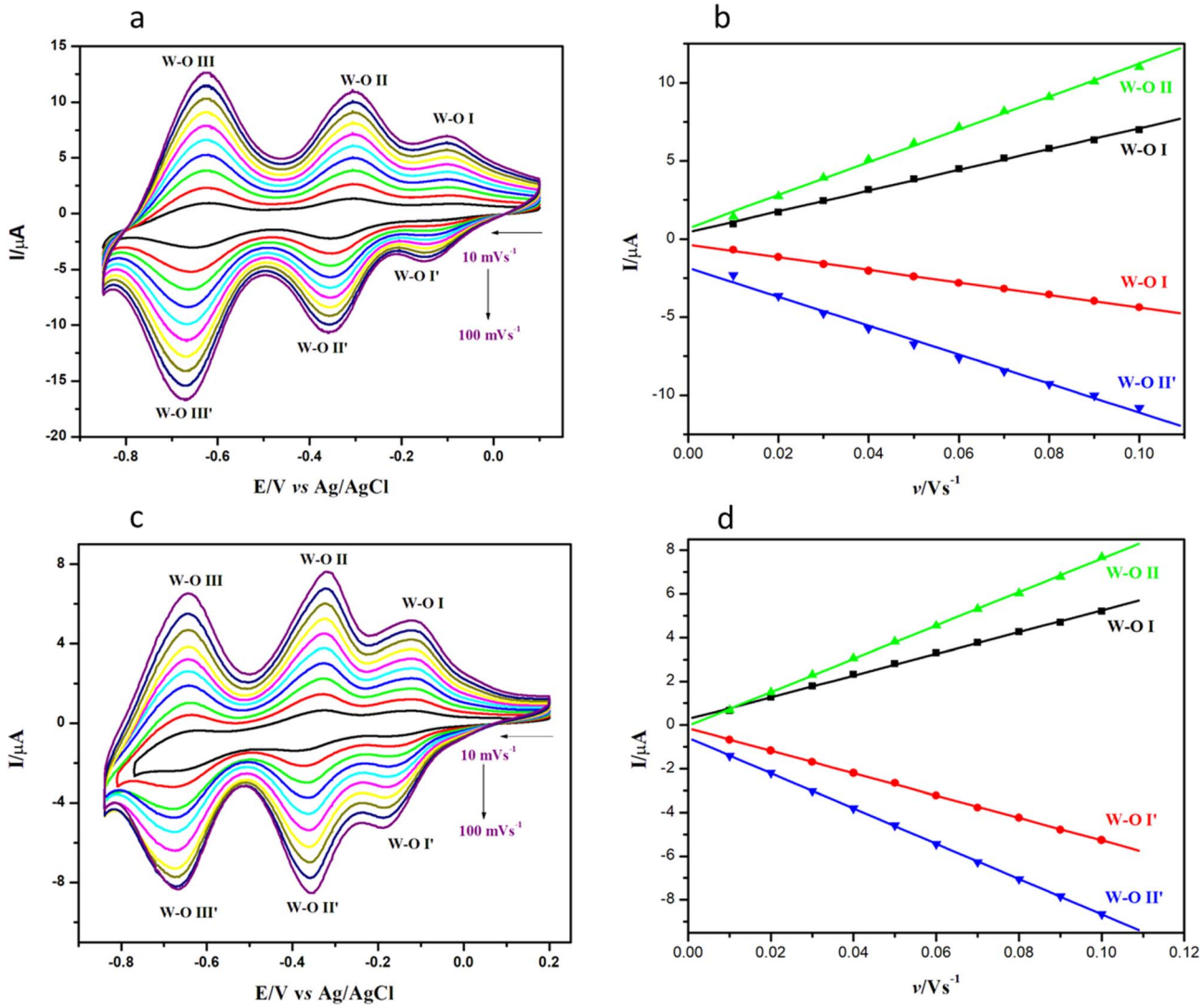

Fig. 3 Cyclic voltammogram of (a) [AuNps-MWCNT/$Mn^{II}_4(P_2W_{15})_2]_4$ and (c) [AuNps-MWCNT/$Mn^{III}_4(P_2W_{15})_2]_4$ modified electrode at different scan rates from 10 mV s^{-1} to 100 mV s^{-1} in pH 2 buffer. Relationship between magnitude in peak currents and the scan rate for (b) [AuNps-MWCNT/$Mn^{II}_4(P_2W_{15})_2]_4$ and (d) [AuNps-MWCNT/$Mn^{III}_4(P_2W_{15})_2]_4$ modified electrode.

Table 1 Slope and regression values for the [AuNps-MWCNT/$Mn^{II}_4(P_2W_{15})_2]_4$ and [AuNps-MWCNT/$Mn^{III}_4(P_2W_{15})_2]_4$ multi-layered modified electrode

	[AuNps-MWCNT/$Mn^{II}_4(P_2W_{15})_2]_4$		[AuNps-MWCNT/$Mn^{III}_4(P_2W_{15})_2]_4$	
Peaks W–O	Slope	R^2	Slope	R^2
I	$y = 66.56x + 0.43$	0.9984	$y = 49.68x + 0.27$	0.9989
I′	$y = -40.35x - 0.36$	0.9989	$y = -51.25x - 0.15$	0.9997
II	$y = 69.51x + 0.11$	0.997	$y = 76.37x - 0.025$	0.9996
II′	$y = -92.64x - 1.85$	0.9926	$y = -80.72x - 0.58$	0.9999

As observed from Fig. 4a and b, an increase in pH causes the POM's peak potentials to shift cathodically with their magnitude in terms of peak current decreasing. The acceptance of protons during the POM reduction processes so as to allow electron delocalisation across the POM accounts for this pH dependence. Peak potential has shifted as a result of POM's inherent tendency to shift when the electrolyte's pH has increased. The $E_{1/2}$ values of peak W–O I, W–O II, and W–O III observed at different pH were plotted as the function of the pH of the electrolyte (Fig. 4b and d). The slope of −86, −77 and −64 mV/pH for the respective peaks W–O I, W–O II, and W–O III were obtained for [AuNps-MWCNT/$Mn^{II}_4(P_2W_{15})_2]_4$ and −78, −77 and −64 mV/pH for the [AuNps-MWCNT/$Mn^{II}_4(P_2W_{15})_2]_4$ multi-layered film, respectively. All the calculated values are closer to the theoretical Nernstian value (−59 mV/pH), show the number of protons and electrons involved in the electron transfer is equal.

Stability is an important parameter for any catalyst in the industrial view. A pH 2 buffer was used to record 200 potential scans that covered every step of the POM's redox process in order to evaluate the cycling stability of the modified electrodes.

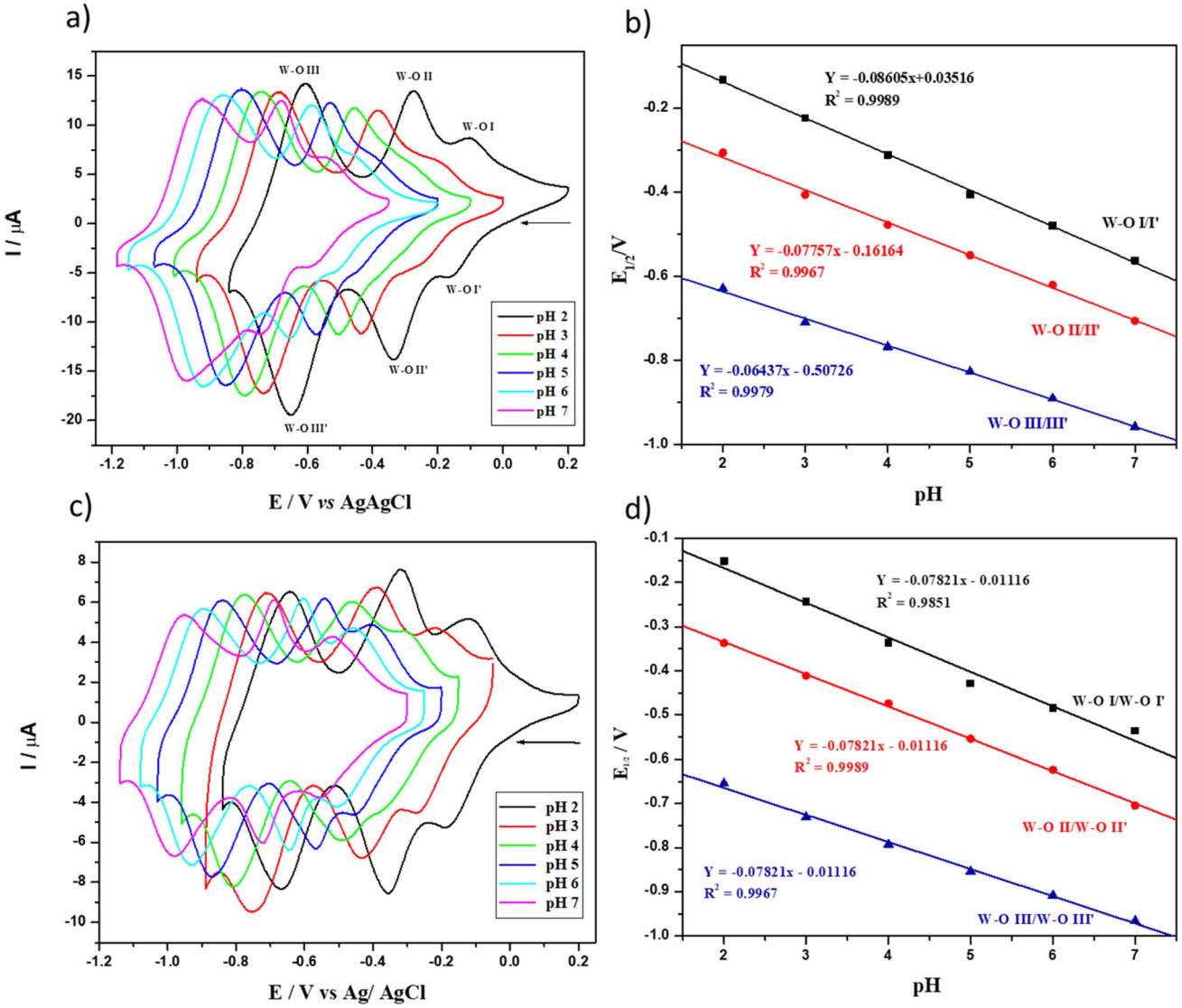

Fig. 4 Cyclic voltammogram (a) [AuNps-MWCNT/$Mn^{II}_4(P_2W_{15})_2]_4$ and (c) [AuNps-MWCNT/$Mn^{III}_4(P_2W_{15})_2]_4$ modified electrode in a buffer solution of different pH of 2–7 at the scan rate of 100 mV s^{-1}. Relationship between the potential of peak W–O I, II and II and pH for (b) [AuNps-MWCNT/$Mn^{II}_4(P_2W_{15})_2]_4$ and (d) [AuNps-MWCNT/$Mn^{III}_4(P_2W_{15})_2]_4$ modified electrode.

As seen in Fig. 5b, the peak current magnitude of the [AuNps-MWCNT/$Mn^{III}_4(P_2W_{15})_2]_4$ modified electrode slightly decreased, especially the current magnitude of W–O III peak, while the peak current magnitude of the [AuNps-MWCNT/$Mn^{II}_4(P_2W_{15})_2]_4$ modified electrode (Fig. 6a) decreased only slightly after 200 cycles. The modified electrodes with multiple layers display stable redox peaks in solutions with various pH levels. The pH study and cycling stability results demonstrate the electrochemical stability of the modified electrodes.

3.3. Electrochemical impedance spectroscopy

EIS is a multifrequency AC electrochemical measurement technique. It measures the electrical resistance (impedance) of the metal/solution interface over a wide range of frequencies. The results obtained in EIS give the possibility for determining the polarization resistance (low-frequency region), the solution resistance (high-frequency region), and the capacitance of the double layer.[61] EIS has been employed to study the change in the electrical properties of the multi-layered films during the LBL assembly process using the ferro/ferricyanide couple as a redox probe. The impedance studies were performed in a 10 mmol L^{-1} potassium ferricyanide and 10 mmol L^{-1} potassium ferrocyanide with 0.1 mol L^{-1} potassium chloride as the electrolyte solution during the layer construction.

The interpretation of impedance data has been carried out through the employment of Randle's equivalent circuit based on the previously published literature. Fig. 7 shows Randle's equivalent circuit, which contains R_s represents the uncompensated solution resistance between the electrolyte and electrode, R_{ct} is the charge transfer resistance, and C_{dl} is the double layer capacitance of the solution in series. In this case of the modified electrode, C_{dl} is replaced by a constant phase

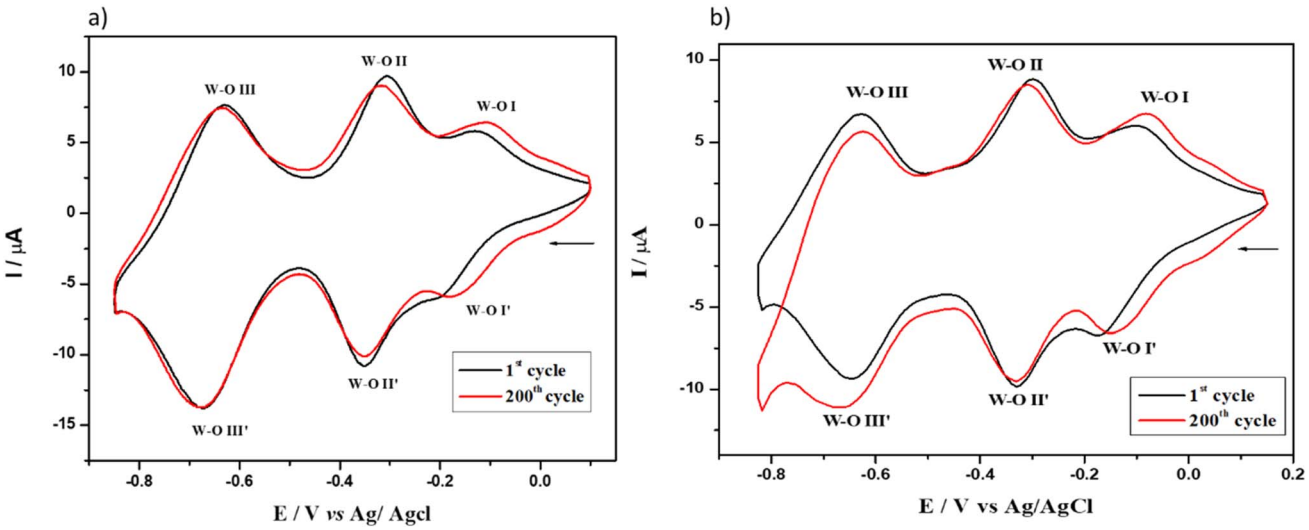

Fig. 5 Continuous cyclic voltammogram of (a) [AuNps-MWCNT/$Mn^{II}_4(P_2W_{15})_2]_4$ and (b) [AuNps-MWCNT/$Mn^{III}_4(P_2W_{15})_2]_4$ modified electrode in pH 2 buffer at the scan rate of 100 mV s^{-1}.

electrode (CPE). The CPE is modelled as a non-ideal capacitor, given by eqn (6)

$$\mathrm{CPE} = -1/(C_i W)^n \quad (6)$$

where C is the capacitance, which describes the charge separation at the double layer interface, ω is the frequency in rad s^{-1} and n exponent is due to the heterogeneity of the surface, $n = 1$ for an ideal capacitor.

Fig. 6a and b shows the Nyquist plot of [AuNps-MWCNT/$Mn^{II}_4(P_2W_{15})_2]_4$ and [AuNps-MWCNT/$Mn^{III}_4(P_2W_{15})_2]_4$ multilayered modified electrodes, respectively. Changes during the stepwise deposition of AuNps-MWCNT and POM are clearly visible in Fig. 6. Regardless of the charge of the transition metal atom, the diameter of the semicircle grows as the number of POM bilayers increases, which can be attributed to the growth in film thickness and the alteration in charge transfer resistance.

The attraction between the anionic POM and the anionic probe used in this study may also be a contributing factor. It is interesting to note that the R_{ct} values significantly drop for each deposition of MWCNT decorated with AuNps. This effect is most likely caused by the high conductivity of the AuNps-decorated MWCNT, which makes it easier for the probe molecules and the altered electrode surface to communicate electronically.

Furthermore, the electrostatic attraction between nanoparticles and the negatively charged ferricyanide/ferrocyanide redox probe can speed up the electrode reaction rate. Finally, using MWCNT may result in non-uniform or defective films with a larger surface area.

Additionally, Fig. 8 shows a plot of the number of layers against the R_{ct} that was generated from the impedance data using the EIS spectrum analyser. Fig. 8 clearly shows the trend of increasing R_{ct} values as the POM layer increases and decreasing R_{ct} values as the AuNps-MWCNT layer increases. A significant observation was the variation in Warburg impedance with each deposition step. This phenomenon could be attributed to changes in the morphology and structure of the layers during the Layer-by-Layer (LbL) assembly process. For instance, the fourth layer may induce a more porous structure compared to the third layer, thereby altering the pathways for ion and electron transport. This change can enhance diffusion processes and subsequently exhibit Warburg impedance characteristics.[62]

3.4. Electrochemical iodate sensor

The [AuNps-MWCNT/$Mn^{II}_4(P_2W_{15})_2]_4$ and [AuNps-MWCNT/$Mn^{III}_4(P_2W_{15})_2]_4$ modified GC electrode was used to detect the iodate in the water. Cyclic voltammogram in Fig. 10a and b, shows the response of the [AuNps-MWCNT/$Mn^{II}_4(P_2W_{15})_2]_4$ and [AuNps-MWCNT/$Mn^{III}_4(P_2W_{15})_2]_4$ modified GC electrode respectively, towards the presence and absence of iodate in pH 2 buffer solution within the potential range of 0.2 to −0.8 V *vs.* Ag/AgCl.

Fig. 9 clearly shows the electrocatalytic reduction of iodate using both modified electrodes. The first two redox peaks W–O I and W–O II correspond to the POM unit participating in the electrochemical reduction of iodate. The reduction current associated with the W–O I and W–O II increases with the increasing concentration of iodate (Fig. S1a and S2a†). The electrochemical response of the bare GC electrode towards the iodate (1 mmol L^{-1}) was also demonstrated in Fig. 9, which shows the poor response of the bare GC electrode towards the iodate. By subtracting the current response of the iodate ion at a given concentration from the current response of the multilayer modified electrode in the absence of an analyte was calculated to find out the relationship between the I_{cat} and the concentration of the analyte (Fig. S1b and S2b†). Fig. S1b and S2b† show the linear relationship between the I_{cat} and the concentration of the iodate (200–2000 μmol L^{-1}) for the [AuNps-

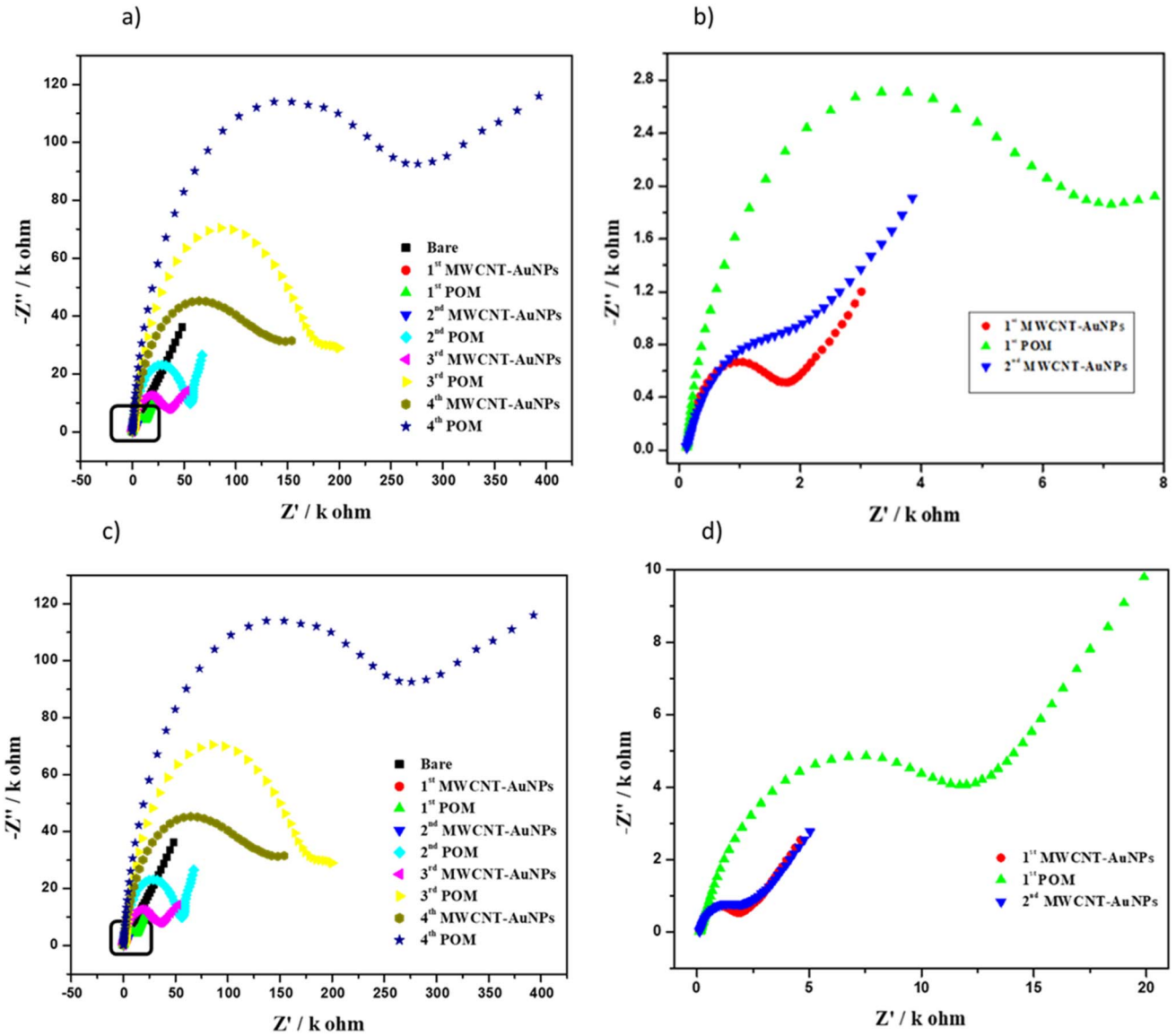

Fig. 6 Nyquist plots of a multilayer film of (a) [AuNps-MWCNT/$Mn^{II}_4(P_2W_{15})_2]_4$ and (c) [AuNps-MWCNT/$Mn^{III}_4(P_2W_{15})_2]_4$ on glassy carbon electrode. (b) and (d) Zoomed view of the Nyquist plot of (a) and (c) respectively. The frequency range is between 0.01 to 10^5 Hz. The amplitude of the applied sine wave potential in each case was 10 mV in the presence of a 10 mmol L^{-1} solution of $K_3[Fe(CN)_6]$ and $K_4[Fe(CN)_6]$ (1 : 1) in 0.1 mol L^{-1} KCl as a redox probe.

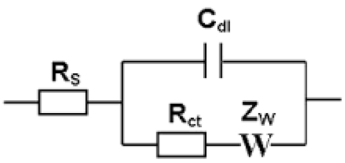

Fig. 7 Randle's equivalent circuit was used to measure the impedance data performed at the modified GC electrode.

MWCNT/$Mn^{II}_4(P_2W_{15})_2]_4$ and [AuNps-MWCNT/$Mn^{III}_4(P_2W_{15})_2]_4$ modified electrodes, respectively. Table 2 includes the sensitivity and LOD as well as the linear range for the voltammetric mode of both modified electrodes.

As expected, the AuNps decorated MWCNT alone modified the GC electrode's amperometric response showing less catalytic activity towards iodate (Fig. 10). Fig. 10 demonstrates that the electrocatalytic activity is caused by the synergistic effect of the catalytic POM and the high electron conductivity of the MWCNT decorated with AuNps. The electrocatalytic reduction potential was noted from the cyclic voltammogram and used as an applied potential for the amperometric detection of iodate in pH 2. Fig. 10(a) and (b) show the resulting amperometric response of the [AuNps-MWCNT/$Mn^{II}_4(P_2W_{15})_2]_4$ and [AuNps-MWCNT/$Mn^{III}_4(P_2W_{15})_2]_4$ modified electrodes respectively, towards the iodate of varying concentration.

As the IO_3^- was added into the stirred pH 2 buffer solution at an optimum potential of −0.35 V, dynamic stairs of the current

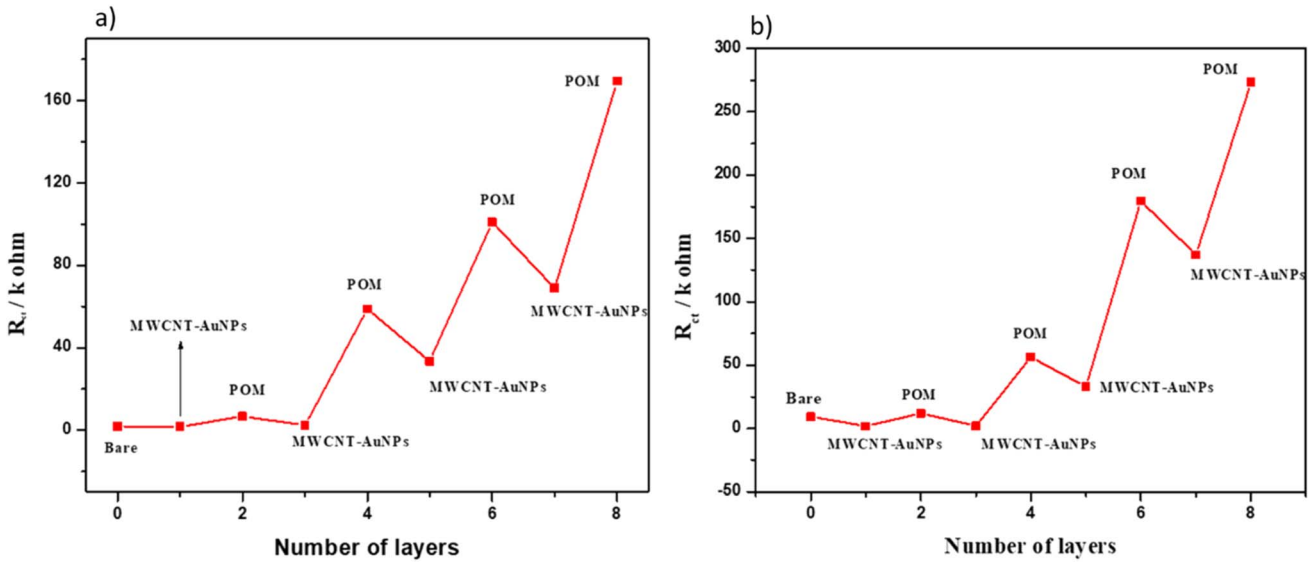

Fig. 8 Dependence of charge transfer resistance (R_{ct}) on the multilayer assembly number in (a) [AuNps-MWCNT/$Mn^{II}_4(P_2W_{15})_2]_4$ and (b) [AuNps-MWCNT/$Mn^{III}_4(P_2W_{15})_2]_4$ based films monitored by impedance spectroscopy.

with quick steady-state were obtained, and the currents increased along with the continuous addition of IO_3^-. This may be caused by the quick diffusion of the IO_3^- small molecules from the solution to the modified electrode's surface and the modifier's improved electron transfer rate, which may both be significant factors. Fig. 10b shows the relation between iodate concentrations (1–8000 μmol L^{-1}) and the corresponding current values. As can be seen, the linear range is from 1–3000 μmol L^{-1} for the [AuNps-MWCNT/$Mn^{II}_4(P_2W_{15})_2]_4$ modified electrode. Similarly, the linear range from 1–3000 μmol L^{-1} was observed for the [AuNps-MWCNT/$Mn^{III}_4(P_2W_{15})_2]_4$ modified electrode (Fig. 10d).

The current response of the [AuNps-MWCNT/$Mn^{II}_4(P_2W_{15})_2]_4$ and [AuNps-MWCNT/$Mn^{III}_4(P_2W_{15})_2]_4$ modified electrodes towards iodate was monitored in the common analytes that typically co-exist in the real samples such as $NaNO_3$, $NaNO_2$, KH_2PO_4, $NaClO_3$, $KBrO_3$, H_2O_2, and KCl (1 mmol L^{-1}) (Fig. 11(a) and (b), respectively).

The current–time response in Fig. 11(a) and (b) obtained after adding interference analytes (1 mmol L^{-1}) successively showed no interference, demonstrating the high selectivity of the modified electrodes for the iodate ion (100 mol L^{-1}) in the presence of interference analytes.

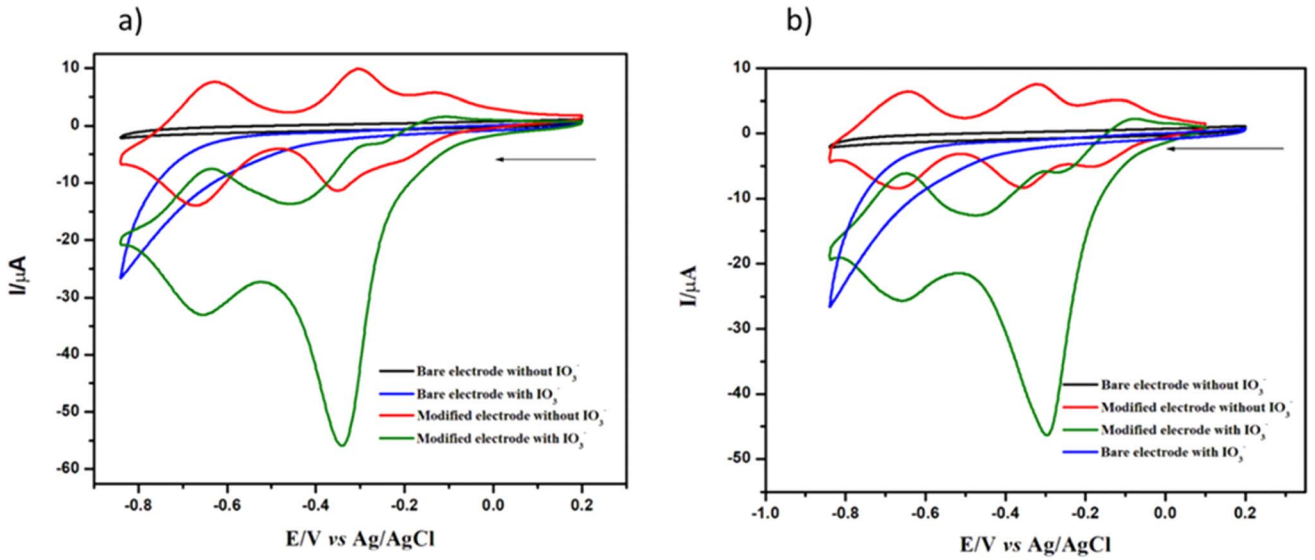

Fig. 9 Cyclic voltammogram of (a) [AuNps-MWCNT/$Mn^{II}_4(P_2W_{15})_2]_4$ and (b) [AuNps-MWCNT/$Mn^{III}_4(P_2W_{15})_2]_4$ modified electrode in the presence and the absence of iodate (1 mmol L^{-1}).

Table 2 Linear range, sensitivity and LOD of the modified electrode[a]

Modified film	Linear range/μM	Sensitivity/μA cm^{-2} μM^{-1}	LOD/μM
[AuNps-MWCNT/$Mn^{II}_4(P_2W_{15})_2]_4$	1–3000	0.58	0.14
[AuNps-MWCNT/$Mn^{III}_4(P_2W_{15})_2]_4$	1–3000	0.90	0.20

[a] LOD: lower limit of detection, AuNPs: gold nanoparticles, MWCNT: multi-walled carbon nanotubes.

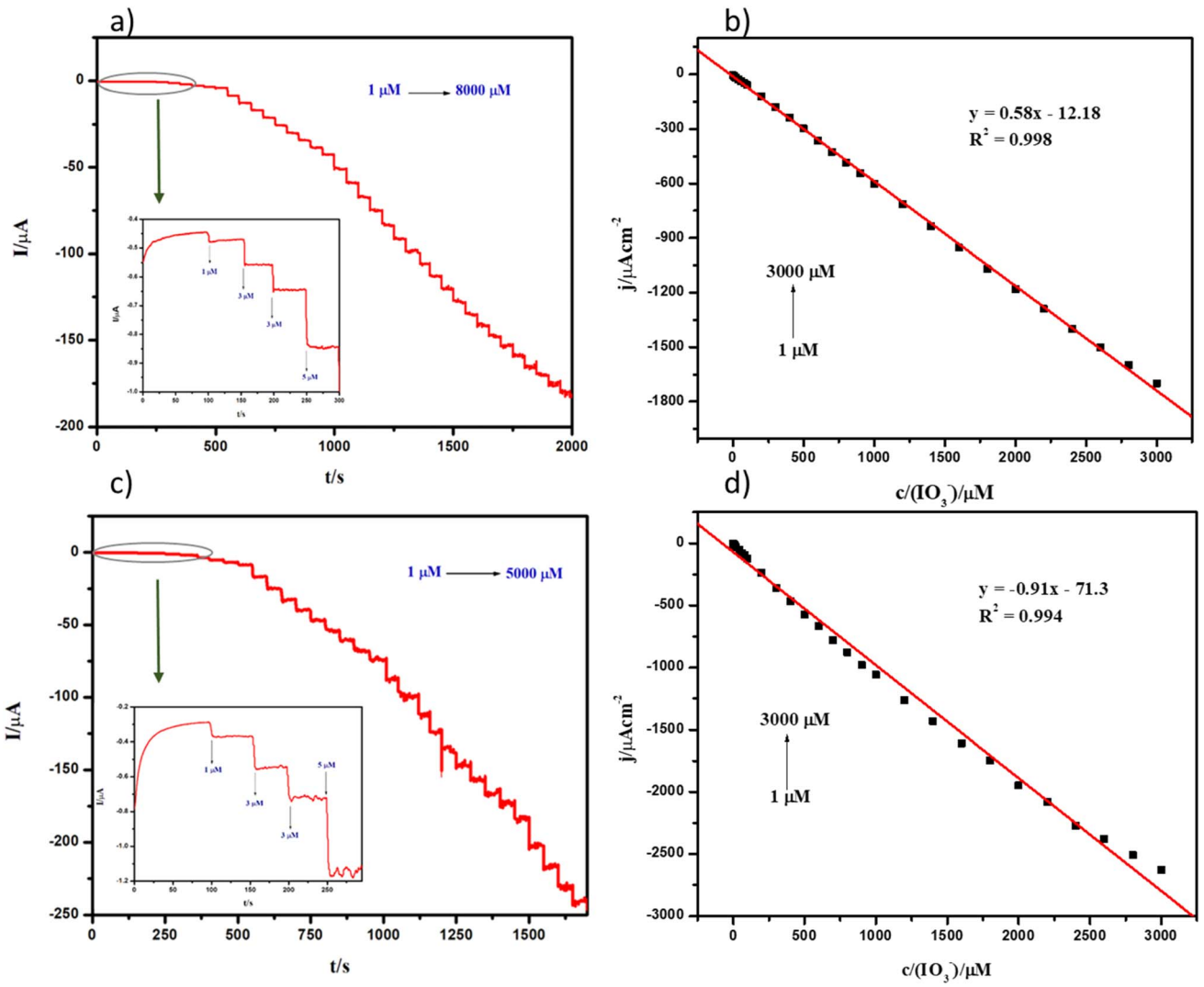

Fig. 10 Amperometric response of the (a) [AuNps-MWCNT/$Mn^{II}_4(P_2W_{15})_2]_4$ and (c) [AuNps-MWCNT/$Mn^{III}_4(P_2W_{15})_2]_4$ modified electrodes towards the increase in the concentration of iodate from 1–8000 μmol L^{-1} and 1–5000 respectively with an applied potential of −0.35 V *vs.* Ag/AgCl. (b) and (d) The relation between the current value and the concentration of the iodate.

4. Surface characterisation

4.1. Atomic force microscopy

The AFM topographic images of [AuNps-MWCNT/$Mn^{II}_4(P_2W_{15})_2]_4$ and [AuNps-MWCNT/$Mn^{III}_4(P_2W_{15})_2]_4$ were presented in the ESI Fig. S3a and b† respectively, confirmed the thin interconnected and regularly distributed layer. The average thickness of [AuNps-MWCNT/$Mn^{II}_4(P_2W_{15})_2]_4$ and [AuNps-MWCNT/$Mn^{III}_4(P_2W_{15})_2]_4$ film was found to be ∼250 nm and ∼225 nm respectively. The presence of globular particles is due to the presence of POM as the outer layer.

4.2. Fourier transform infrared spectroscopy (FTIR)

Fourier-transform infrared (FT-IR) spectroscopy was performed on both the powder samples and the [AuNps-MWCNT/$Mn^{II}_4(P_2W_{15})_2]_4$ and [AuNps-MWCNT/$Mn^{III}_4(P_2W_{15})_2]_4$ films formed on ITO-coated glass slides. Fig. S4a and b† present the FT-IR

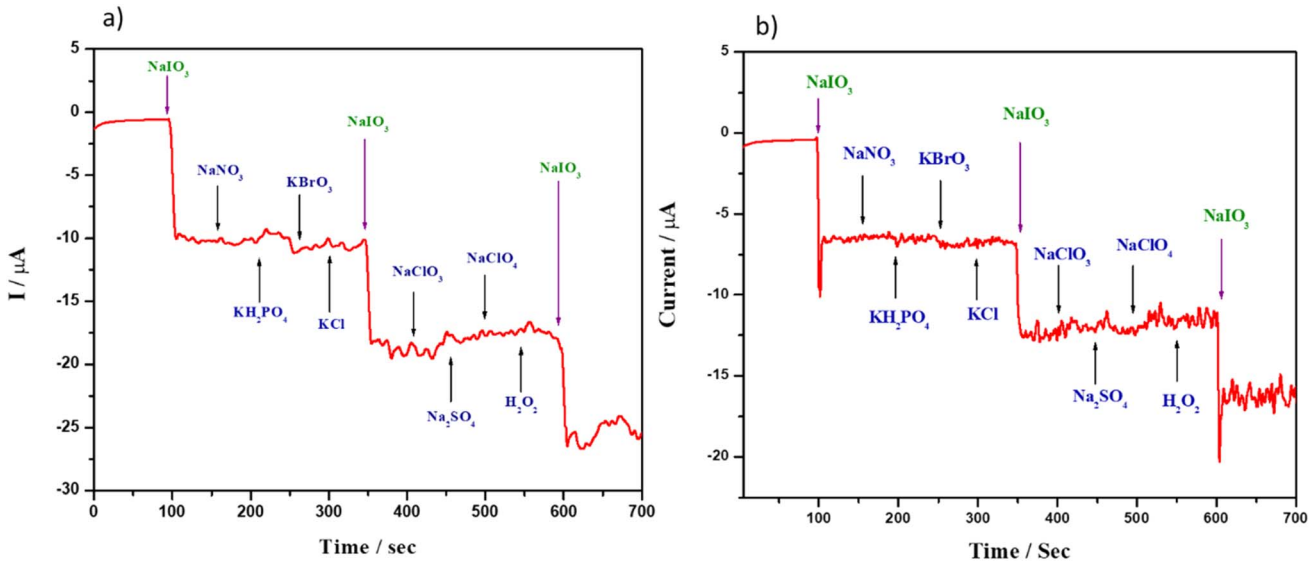

Fig. 11 The amperometric response of the (a) [AuNps-MWCNT/$Mn^{II}_4(P_2W_{15})_2]_4$ and (b) [AuNps-MWCNT/$Mn^{III}_4(P_2W_{15})_2]_4$ towards the iodate (100 µmol L^{-1}) with the presence of various interference analytes (1 mmol L^{-1}) at the polarization potential of −0.35 v *vs.* Ag/AgCl.

spectra for the [AuNps-MWCNT/$Mn^{II}_4(P_2W_{15})_2]_4$ and [AuNps-MWCNT/$Mn^{III}_4(P_2W_{15})_2]_4$ films along with their respective powder samples. For the thiolated MWCNTs, a peak near 3450 cm^{-1} corresponds to the symmetric N–H vibration of amine groups. Broad bands observed at approximately 1616 cm^{-1} and 1509 cm^{-1} were attributed to the overlapping of COO^- stretching modes and NH_3^+ bending vibrations, indicative of the presence of protonated amino groups. This supports the formation of zwitterionic species through the deprotonation of carboxyl (–COOH) groups, confirming successful thiol group grafting onto the MWCNT surface.

Characteristic P–O stretching vibrations for $Mn^{II}_4(P_2W_{15})_2$ were observed at 1091 cm^{-1} and 1047 cm^{-1}, whereas $Mn^{III}_4(P_2W_{15})_2$ exhibited similar stretching modes at 1080 cm^{-1} and 1048 cm^{-1}. Terminal W=O stretches appeared at 930 cm^{-1} for $Mn^{II}_4(P_2W_{15})_2$ and 940 cm^{-1} for $Mn^{III}_4(P_2W_{15})_2$. Additionally, W–O–W bridging vibrations were identified at 919 cm^{-1} and 706 cm^{-1}. These characteristic peaks were retained in the Layer-by-Layer (LbL) constructed [AuNPs-MWCNT/$Mn^{II}_4(P_2W_{15})_2]_4$ and [AuNPs-MWCNT/$Mn^{III}_4(P_2W_{15})_2]_4$ films, demonstrating the successful integration of AuNPs-MWCNT and polyoxometalates (POMs) into the layered structures.[63,64]

5. Conclusion

A simple and efficient Layer-by-Layer (LbL) approach to assemble the sandwich structured $[M_4(H_2O)_2(P_2W_{15}O_{56})_2]^{n-}$ (M = Mn^{II} And Mn^{III}) polyoxometalates (POMs) with gold nanoparticles (AuNps) decorated multi-walled carbon nanotubes (MWCNT) on the surface of the glassy carbon electrode has been represented. The fabricated multilayer assemblies were characterised by cyclic voltammetry and electrochemical impedance spectroscopy (EIS) techniques. The pH depend redox activity was observed across a range of pH 2 to 7 for the multilayer assemblies. With the rise in pH, the W–O redox pairs of the POM changed toward more negative potentials. Electrochemical impedance spectroscopy was also employed to the multilayer system during the layer construction. It was observed that the value for the charge transfer resistance increased with layer number and also was dependent upon the nature of the terminal layer of the multilayer film. The preliminary study using cyclic voltammetry for the electrocatalytic reduction of iodate revealed that the films had the capacity to considerably decrease the iodate. The electrocatalytic activity of the film was also investigated by amperometry techniques. The amperometric response time was calculated to be less than 5 s, supporting the thin film's faster electron transfer rate. It also shows how well iodate can be detected even in the presence of several interfering analytes.

Data availability

Data shall be made available on request.

Conflicts of interest

There are no conflicts to declare.

References

1 S. Liu and Z. Tang, *Nano Today*, 2010, **5**, 267–281.
2 S. Herrmann, C. Ritchie and C. Streb, *Dalton Trans.*, 2015, **44**, 7092–7104.
3 T. Ueda, *Anal. Sci.*, 2021, **37**, 107–118.
4 M. Samaniyan, M. Mirzaei, R. Khajavian, H. Eshtiagh-Hosseini and C. Streb, *ACS Catal.*, 2019, **9**, 10174–10191.
5 J. J. Ye and C. De Wu, *Dalton Trans.*, 2016, **45**, 10101–10112.

6 A. Proust, R. Thouvenot and P. Gouzerh, *Chem. Commun.*, 2008, 1837–1852.
7 E. Papaconstantinou, *Chem. Soc. Rev.*, 1989, **18**, 1–31.
8 R. Sivakumar, J. Thomas and M. Yoon, *J. Photochem. Photobiol., C*, 2012, **13**, 277–298.
9 J. T. Rhule, C. L. Hill, D. A. Judd and R. F. Schinazi, *Chem. Rev.*, 1998, **98**, 327–357.
10 D. M. Fernandes, C. M. A. Brett and A. M. V. Cavaleiro, *J. Electroanal. Chem.*, 2011, **660**, 50–56.
11 U. Kortz, A. Müller, J. van Slageren, J. Schnack, N. S. Dalal and M. Dressel, *Coord. Chem. Rev.*, 2009, **253**, 2315–2327.
12 D. L. Long, R. Tsunashima and L. Cronin, *Angew. Chem., Int. Ed.*, 2010, **49**, 1736–1758.
13 T. Ueda, *ChemElectroChem*, 2018, **5**, 823–838.
14 V. Pifferi, A. Testolin, C. Ingrosso, M. L. Curri, I. Palchetti and L. Falciola, *Chemosensors*, 2022, **10**(2), 67.
15 S. Chen, R. Yuan, Y. Chai and F. Hu, *Microchim. Acta*, 2013, **180**, 15–32.
16 Z. Xian, R. Liu, H. Li, S. Zhang, Z. Yang, W. Zheng, C. Chen, H. Cao and G. Zhang, *J. Cluster Sci.*, 2016, **27**, 241–256.
17 J. Gong, T. Zhou, D. Song and L. Zhang, *Sens. Actuators, B*, 2010, **150**, 491–497.
18 X. D. Hong, D. Liang, P. Z. Wu and H. R. Zheng, *Diamond Relat. Mater.*, 2016, **69**, 61–67.
19 P. K. Sandhya, J. Jose, M. S. Sreekala, M. Padmanabhan, N. Kalarikkal and S. Thomas, *Ceram. Int.*, 2018, **44**, 15092–15098.
20 A. Z. Ernst, S. Zoladek, K. Wiaderek, J. A. Cox, A. Kolary-Zurowska, K. Miecznikowski and P. J. Kulesza, *Electrochim. Acta*, 2008, **53**, 3924–3931.
21 Y. Han, Y. Xiao, Z. Zhang, B. Liu, P. Zheng, S. He and W. Wang, *Macromolecules*, 2009, **42**, 6543–6548.
22 M. Clemente-León, E. Coronado, C. J. Gómez-García, C. Mingotaud, S. Ravaine, G. Romualdo-Torres and P. Delhaès, *Chem.–Eur. J.*, 2005, **11**, 3979–3987.
23 M. Clemente-León, B. Agricole, C. Mingotaud, C. J. Gómez-García, E. Coronado and P. Delhaes, *Langmuir*, 1997, **13**, 2340–2347.
24 K. Ariga, E. Ahn, M. Park and B. S. Kim, *Chem.–Asian J.*, 2019, **14**, 2553–2566.
25 D. Kim, M. Gu, M. Park, T. Kim and B. S. Kim, *Mol. Syst. Des. Eng.*, 2019, **4**, 65–77.
26 K. Ariga, Y. Yamauchi, G. Rydzek, Q. Ji, Y. Yonamine, C. W. Kevin and J. P. Hill, *Chem. Lett.*, 2014, **43**, 36–68.
27 M. Ammam, *J. Mater. Chem. A*, 2013, **1**, 6291–6312.
28 M. Ammam, B. Keita, L. Nadjo, I. M. Mbomekalle and J. Fransaer, *J. Electroanal. Chem.*, 2010, **645**, 65–73.
29 I. Sakthinathan, J. Köhling, V. Wagner and T. McCormac, *ACS Appl. Mater. Interfaces*, 2023, **15**, 2861–2872.
30 H. Li, S. Pang, S. Wu, X. Feng, K. Müllen and C. Bubeck, *J. Am. Chem. Soc.*, 2011, **133**, 9423–9429.
31 B. Ali, T. McCormac, E. Lepleux, L. Pacheco, F. Laffir and C. Maccato, *Electrochim. Acta*, 2020, **343**, 1–12.
32 M. A. Sahebalzamani, T. Sadat Hashemi, Z. Mousavi Nejad, S. Agarwal, H. O. McCarthy, T. J. Levingstone and N. J. Dunne, *Mater. Adv.*, 2024, 2316–2327.
33 J. Borges, J. Zeng, X. Q. Liu, H. Chang, C. Monge, C. Garot, K. feng Ren, P. Machillot, N. E. Vrana, P. Lavalle, T. Akagi, M. Matsusaki, J. Ji, M. Akashi, J. F. Mano, V. Gribova and C. Picart, *Adv. Healthcare Mater.*, 2024, **2302713**, 1–28.
34 J. Lipton, G. M. Weng, J. A. Röhr, H. Wang and A. D. Taylor, *Matter*, 2020, **2**, 1148–1165.
35 S. Zhao, F. Caruso, L. Dahne, G. Decher, B. G. De Geest, J. Fan, N. Feliu, Y. Gogotsi, P. T. Hammond, M. C. Hersam, A. Khademhosseini, N. Kotov, S. Leporatti, Y. Li, F. Lisdat, L. M. Liz-Marzan, S. Moya, P. Mulvaney, A. L. Rogach, S. Roy, D. G. Shchukin, A. G. Skirtach, M. M. Stevens, G. B. Sukhorukov, P. S. Weiss, Z. Yue, D. Zhu and W. J. Parak, *ACS Nano*, 2019, **13**, 6151–6169.
36 H. Ravanbakhsh and S. Dianat, *Sens. Bio-Sens. Res.*, 2023, **40**, 100556.
37 H. F. Galiga and F. B. Sevilla, *Food Chem.*, 2023, **414**, 135741.
38 A. Yaqub, M. Vagin, J. J. Walsh, F. Laffir, I. Sakthinathan, T. McCormac and M. Yaqub, *ACS Omega*, 2022, **7**, 43381–43389.
39 H. Chen, Q. Li, B. Hu, W. Zhu, H. Xia and W. Yang, *Talanta*, 2023, **261**, 124661.
40 M. A. Jamilan, J. Abdullah, S. A. Alang Ahmad and M. F. Md Noh, *Food Chem.*, 2022, **393**, 133382.
41 L. Guadagnini and D. Tonelli, *Sens. Actuators, B*, 2013, **188**, 806–814.
42 X. Huang, Y. Li, Y. Chen and L. Wang, *Sens. Actuators, B*, 2008, **134**, 780–786.
43 A. Salimi, A. Noorbakhsh and M. Ghadermarzi, *Sens. Actuators, B*, 2007, **123**, 530–537.
44 X. Zhang, Y. Bao, Y. Bai, Z. Chen, J. Li and F. Feng, *Electrochim. Acta*, 2019, **300**, 380–388.
45 A. Yaqub, S. R. Gilani, S. Bilal, A. Hayat, A. Asif and S. A. Siddique, *ACS Omega*, 2022, **7**, 149–159.
46 M. Sharifi, S. Dianat and A. Hosseinian, *RSC Adv.*, 2021, **11**, 8993–9007.
47 Y. Pan, L. Wang, S. Chen, Y. Wei and X. Wei, *Food Chem.*, 2024, **440**, 138185.
48 D. Minta, Z. González and G. Gryglewicz, *Chem. Eng. Sci.*, 2024, **292**, 120009.
49 Y. Liu, X. Yan, Y. Xing, P. Zhao, Y. Zhu, L. Li, N. Liu and Z. Zhang, *ACS Appl. Nano Mater.*, 2024, **7**, 4980–4988.
50 I. S. Marques, B. Jarrais, S. M. Mbomekallé, A. L. Teillout, P. De Oliveira, C. Freire and D. M. Fernandes, *Catalysts*, 2022, **12**(4), 440.
51 R. G. Finke, M. W. Droege and P. J. Domaillezb, *Inorg. Chem.*, 1987, **26**, 3886–3896.
52 T. Lis, *Acta Crystallogr., Sect. B*, 1980, **36**, 2042–2046.
53 C. J. Gómez-García, J. J. Borrás-Almenar, E. Coronado and L. Ouahab, *Inorg. Chem.*, 1994, **33**, 4016–4022.
54 J. Zhu, J. D. Kim, H. Peng, J. L. Margrave, V. N. Khabashesku and E. V. Barrera, *Nano Lett.*, 2003, **3**, 1107–1113.
55 K. Balasubramanian and M. Burghard, *Small*, 2005, **1**, 180–192.
56 V. Duc Chinh, G. Speranza, C. Migliaresi, N. Van Chuc, V. Minh Tan and N. T. Phuong, *Sci. Rep.*, 2019, **9**, 1–9.

57 M. Lebrini, I. M. Mbomekallé, A. Dolbecq, J. Marrot, P. Berthet, J. Ntienoue, F. Sécheresse, J. Vigneron and A. Etcheberry, *Inorg. Chem.*, 2011, **50**, 6437–6448.
58 J. Goura, M. Choudhari, T. Nisar, T. Balster, J. K. Bindra, J. Kinyon, B. Ali, T. McCormac, N. S. Dalal, V. Wagner and U. Kortz, *Inorg. Chem.*, 2020, **59**, 13034–13041.
59 B. Ali, I. Sakthinathan, D. Barreca, C. Maccato, J. Goura, U. Kortz and T. McCormac, *Thin Solid Films*, 2023, **766**, 139610.
60 N. Elgrishi, K. J. Rountree, B. D. McCarthy, E. S. Rountree, T. T. Eisenhart and J. L. Dempsey, *J. Chem. Educ.*, 2018, **95**, 197–206.
61 A. C. Lazanas and M. I. Prodromidis, *ACS Meas. Sci. Au*, 2023, **3**, 162–193.
62 F. X. Xiao, M. Pagliaro, Y. J. Xu and B. Liu, *Chem. Soc. Rev.*, 2016, **45**, 3088–3121.
63 G. A. D. Castro, N. P. G. Lopes, S. A. Fernandes and M. J. Silva, *Cellulose*, 2022, **29**, 5529–5545.
64 J. Raabe, F. Jarneel, M. Stein, J. Albert and M. J. Poller, *Dalton Trans.*, 2021, **59**, 454.